

Squeezing and correlations of multiple modes in a parametric acoustic cavity

Gustav Andersson,^{1,*} Shan W. Jolin,² Marco Scigliuzzo,¹ Riccardo Borgani,² Mats O. Tholén,^{2,3} David B. Haviland,² and Per Delsing¹

¹*Department of Microtechnology and Nanoscience MC2,
Chalmers University of Technology, SE-41296 Göteborg, Sweden*

²*Nanostructure Physics, KTH Royal Institute of Technology, SE-10691 Stockholm, Sweden*

³*Intermodulation Products AB, SE-82393 Segersta, Sweden*

(Dated: November 18, 2021)

Exploiting multiple modes in a quantum acoustic device could enable applications in quantum information in a hardware-efficient setup, including quantum simulation in a synthetic dimension and continuous-variable quantum computing with cluster states. We introduce a nonlinearity to a multimode surface acoustic wave (SAW) resonator by integrating a superconducting quantum interference device (SQUID) in one of the Bragg reflectors. The interaction with the SQUID-shunted mirror gives rise to coupling between the more than 20 accessible resonator modes. We exploit this coupling to demonstrate two-mode squeezing of SAW phonons, as well as five-mode correlations. Our results demonstrate the feasibility of generating acoustic cluster states, providing a compact physical system for continuous-variable quantum computing.

I. INTRODUCTION

Quantum computation and simulation show potential for tackling difficult computational problems by leveraging superposition and entanglement in engineered quantum devices. Although individual quantum systems can be controlled with excellent precision, scaling the hardware to the complexity required while maintaining sufficient control remains a challenging problem. Most architectures proposed for quantum simulation and computation [1–5] use one circuit component for each node in the processor, leading to demanding hardware requirements for practical applications. It is therefore attractive to explore alternative approaches to quantum computing that provide for compact encoding and processing of quantum information.

In principle, the use of continuous variables (CV) allows for realizations of measurement-based quantum computing with frequency combs, requiring only a small number of coupled quantum systems [6, 7]. This paradigm of quantum computing relies on entangling a large number of modes rather than qubits, and does not face fundamental restrictions preventing universality and fault-tolerance [8]. Much experimental progress in CV encoding of quantum information has been achieved in the domain of quantum optics [9–13], where optical parametric oscillators can be used to generate large cluster states, a type of multipartite entangled states providing the resource for CV quantum computation. In superconducting circuit experiments CV encoding has been pursued mainly for error-correction schemes on logical qubits encoded in many-photon superconducting cavity states [14, 15]. While parametric devices are important for low-noise amplification [16], multimode measurement-based schemes for quantum computing at microwave frequen-

cies have received relatively little attention [17–19]. The dominant approach to quantum computation with superconducting quantum circuits has been the gate-based quantum processor, with most effort expended on scaling up the number of physical qubits [20].

A limiting factor for realizing CV encoding in circuit quantum electrodynamic (QED) systems is the typically large electromagnetic mode spacing, making devices with a large number of accessible modes very long or difficult to design. On the other hand, microwave frequencies are amenable to digital signal processing and thereby a greater degree of programmable control than is currently possible in optical systems. The prospect of integrating superconducting qubits as a means of providing non-Gaussian operations necessary for quantum advantage in computation [21] is an additional strength of microwave circuits.

We demonstrate an approach towards realizing CV quantum computation based on cluster state generation and control in a multi-mode hybrid superconducting quantum acoustic device. Surface acoustic wave (SAW) resonators support dense mode spectra with high Q-factors ($> 10^5$) and have been used in multi-mode experiments in the quantum regime [22–24]. Substantial progress has also been made in recent years in the controlled generation of non-classical phononic states [25–27], and applications as quantum random access memories have been proposed [28]. We introduce a nonlinearity to a SAW resonator by integrating a superconducting quantum interference device (SQUID) into one of the Bragg reflectors. The SQUID inductance modulates the reflectivity of a unit cell in the mirror and hence the effective length of the resonator. Due to the narrow free spectral range, the SQUID reflector gives rise to coupling of more than 20 modes. We exploit this coupling to generate two-mode squeezed states between phonons in different SAW modes. Our results suggest this quantum acoustic platform can be used to create highly entangled multimode states for CV quantum computing. Another

* gustav.andersson@chalmers.se

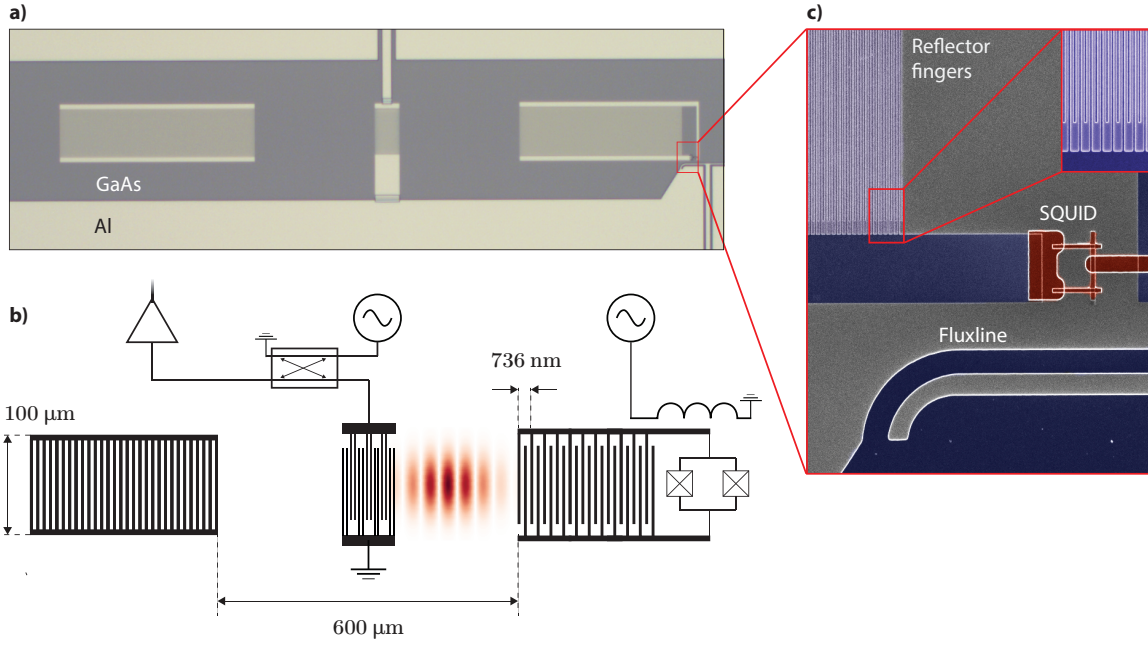


FIG. 1. Device layout. **a)** Optical microscope image of the hybrid SAW resonator. The left Bragg reflector has 1200 fingers all shorted together. The nonlinearity is provided by the reflector on the right hand side, which has 500 unit cells of fingers alternately connected to either the top or bottom electrode, similarly to an IDT. As shown schematically in **b**), the electrodes are shunted by a SQUID. The IDT at the center provides a single input and output port to the resonator. The unit cell of the IDT has a period of 736 nm and a double finger structure to suppress mechanical reflections. **c)** False-color scanning electron micrograph of the right hand side reflector with the SQUID and on-chip fluxline.

possible application for multimode systems is in quantum simulation where the frequency domain may be used as a synthetic dimension [29].

II. DEVICE DESIGN AND SETUP

The SAW resonator, shown in Fig. 1, is defined by two reflectors with the leading edges separated by a distance of 600 μm . The reflector on the left hand side has $N = 1200$ fingers all shorted together. On the right hand side, the reflector has an interdigitated structure, where fingers are connected to either the top or bottom electrode in an alternating pattern. The top and bottom electrodes each have 500 fingers (total $N = 1000$) and are connected via a SQUID. An interdigitated transducer (IDT) centered between the reflectors provides a single port to the resonator. The port IDT has 75 periods and a double-finger structure to suppress mechanical reflections [30]. An on-chip fluxline is used to apply an RF flux through the SQUID. The IDT and reflectors are fabricated from aluminium on a gallium arsenide substrate. Due to the piezoelectric coupling, the SAW field inside the resonator induces an electric potential difference between the top and bottom electrodes, generating currents through the SQUID.

Configurations where an interdigitated reflector is shunted by a variable load impedance have been used for

SAW-based sensors [31]. Here, the SQUID impedance provides a means of flux tuning the SAW resonator, as well as a cross-Kerr interaction between the modes. Integrating the SQUID makes the device a kind of acoustic analogue to the superconducting cavity-based Josephson parametric amplifier [16], where the short wavelength of sound allows for a much denser mode spacing than in the purely electromagnetic case. The SQUID reflector is equivalent to a dispersively coupled nonlinear resonator, as the interdigitated fingers give rise to a large capacitance connected in parallel with the SQUID inductance. We use this model to explain the effect of parametric modulation in this system.

The mode structure of the resonator is shown in Fig. 2. While the IDT is centered with respect to the leading edge of each reflector, the broken symmetry due to the SQUID allows coupling to both odd and even modes with a free spectral range of $FSR = 2.3$ MHz. The alternating pattern of even and odd modes is apparent in the external and internal quality factors Q_c, Q_i extracted from fits to reflection measurements. The IDT couples more effectively to the even modes, resulting in a lower Q_c . The frequency dependence of the IDT and mirrors provide a bandwidth of around 40 MHz around the IDT center frequency where SAW modes are overcoupled.

The narrow free spectral range of the resonator allows for simultaneous measurement of the response at multiple resonances all multiplexed in a single channel.

For this measurement we use a new digital microwave measurement platform called Vivace [32, 33] capable of direct digital synthesis and measurement of frequency combs without analog mixers for frequency conversion. A tuned set of frequencies is used to detect the output of both quadratures of multiple tones, while ensuring a common phase reference. The elimination of analog up and downconversion chains greatly simplifies the scaling up of controllable quantum processors.

III. COUPLED PARAMETRIC RESONATOR INTERACTION

In addition to acting as an efficient SAW reflector, the SQUID mirror supports a lumped-element LC resonance due to the capacitance C of the interdigitated finger structure connected in parallel with the Josephson inductance L_J . This Kerr-nonlinear mode has a frequency of $\omega_{LC} = 2\pi \cdot 3.74$ GHz and couples dispersively to each mode ω_i in the SAW resonator with a coupling strength much smaller than the detuning $g_i \ll \omega_i - \omega_{LC}$. We consider the case where the mirror mode is parametrically modulated but approximately remaining in the ground state, similar to the established scheme for implementing two-qubit gates [34, 35]. In the dispersive regime with the mirror mode adiabatically eliminated, this interaction gives rise to the effective Hamiltonian [33]

$$H/\hbar = \sum_i \left[\omega_i b_i^\dagger b_i + \frac{\bar{g}_i}{2} (\sigma_+^2 + \sigma_-^2) \right] - \frac{1}{2} \sum_{i,j} \tilde{g}_i (b_i + b_i^\dagger) (b_j + b_j^\dagger). \quad (1)$$

Here b_i and b_i^\dagger are the ladder operators for the SAW modes satisfying the commutation relation $[b_i, b_j^\dagger] = \delta_{ij}$, while σ_+ and σ_- refer to the mirror mode. Assuming a uniform vacuum coupling strength g , the effective coupling rates \tilde{g}_i and \bar{g}_i depend on the mirror and SAW mode resonance frequencies as

$$\tilde{g}_i = g^2 (1/(\omega_{LC} - \omega_i) - 1/(\omega_{LC} + \omega_i)), \quad (2)$$

$$\bar{g}_i = g^2 (1/(\omega_{LC} - \omega_i) + 1/(\omega_{LC} + \omega_i)). \quad (3)$$

Because of the double sum in Eq. 1 the interaction between two SAW modes i and j involves both \tilde{g}_i and \tilde{g}_j . Depending on the modulation frequency, either the two-mode squeezing terms or beamsplitter interaction terms will be important. A beamsplitting interaction may be implemented by a parametric drive close to the difference frequency of SAW modes. Modulating near the sum frequency will induce two-mode squeezing between pairs of modes. In our experiment we modulate the magnetic flux through the SQUID with the frequency of a SAW mode without DC flux bias [33]. The parabolic dependence of the frequency on flux implies the mirror mode, and hence

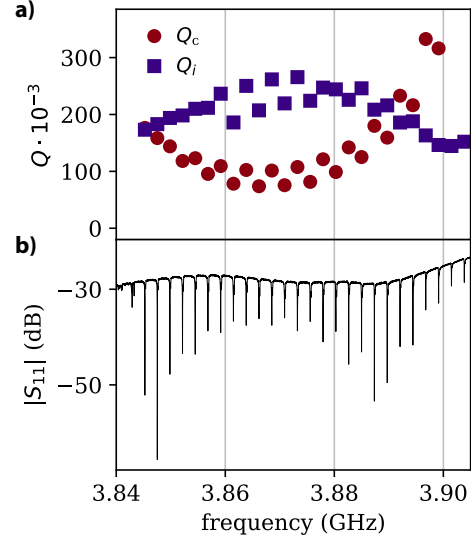


FIG. 2. **Resonator characterization.** a) External and internal quality factors for each mode in the comb. Modes near the center of the 26-mode comb are overcoupled ($Q_c < Q_i$) and have internal quality factors $Q_i > 10^5$ at high power. b) Reflection coefficient measured from the IDT with a vector network analyzer. The alternating even and odd mode pattern as well as the frequency dependence of the IDT response and mirror stopband are visible in the magnitude of resonance dips.

the effective coupling rate, are modulated at twice the pump frequency as $\tilde{g}_i = \tilde{g}_{i,0} + \tilde{g}_{i,1} \cos(2\omega_p t + \theta_p)$. While the excitation of the mirror mode is suppressed in the dispersive regime, it cannot be excluded with certainty considering the linewidth is of the order ~ 10 MHz. The observed squeezing may therefore not be purely an effect of flux-pumping but also involve a contribution from current-pumping.

IV. TWO-MODE SQUEEZING

To observe two-mode squeezing of the SAW field, we apply a parametric pump via the on-chip fluxline at the frequency of a SAW mode f_p . We measure the output field from the IDT at SAW mode frequencies symmetrically around the pump $f_{i,\pm}$, such that $2f_p - f_{i,-} - f_{i,+} = 0$. The frequency configuration of the measurement is illustrated in Fig. 3a. To characterize the correlations, we obtain reference histograms of the I and Q quadratures with the pump turned off. To minimize the effect of slow drift in the experimental setup, the pump output is switched on and off at a rate of 2 Hz. The output signal is amplified using a travelling-wave parametric amplifier [36]. Data are collected over approximately 7 hours (3.5 hours each with the pump on and off). A quadrature rotation is applied to the measured data to compensate for slow phase drift in the experiment.

In Fig. 3b we show subtracted quadrature histograms measured simultaneously in four pairs of SAW modes. Histograms are generated from $N = 1.25 \cdot 10^6$ points measured in each mode with the pump on (off). The unsqueezed histograms obtained with the pump off are then subtracted from those produced with the pump on. We observe squeezing below the pump off level in all four mode pairs, extending the two-mode squeezing effect to SAW phonon fields. The ellipticity, defined as the ratio of the squeezed and anti-squeezed axes

$$R_e = \frac{\sigma_{\max}}{\sigma_{\min}} = \frac{\sqrt{\langle (I_+ + I_-)^2 \rangle}}{\sqrt{\langle (I_+ - I_-)^2 \rangle}} \quad (4)$$

is well above unity for all four mode pairs and shows a diminishing trend with increased detuning. The ratio of the standard deviation in the squeezed quadrature to the pump off case, given by

$$R_p = \frac{\sigma_{\min}}{\sigma_{\text{off}}} = \frac{\sqrt{\langle (I_+ - I_-)^2 \rangle}}{\sqrt{\langle (I_{\text{off}})^2 \rangle}}, \quad (5)$$

has a value $R_p < 1$ across the four mode pairs. The correlation ratios are plotted as a function of pump-probe detuning in Fig. 3c. As expected, no correlations are observed outside the two-mode squeezed pairs [33]. From our analysis of mode correlations (see supplementary material) we estimate that the squeezing is below the vacuum level, if the modes are cooled below an effective temperature of 80 mK. Even if our device is not perfectly thermalized to the 10 mK cryostat temperature, it is unlikely the effective phonon temperature should exceed this bound, leading to the conclusion that we have observed squeezing below the vacuum in the phonon field.

V. MULTIMODE CORRELATIONS

We apply two simultaneous pumps at frequencies $f_{p,1}$ and $f_{p,2}$, corresponding to two different SAW modes. The dual pump scheme gives rise to intermodulation products at the frequencies $f_{IMP} = n_1 f_{p,1} + n_2 f_{p,2}$. As we are interested in cluster state entanglement, we restrict the measured f_k modes to frequencies without either a pump or intermodulation product when analyzing correlations. Two pumps enable multiple phonon down-conversion paths, implying mutual correlation of all measured modes f_k . This scheme can readily be extended to a full pump comb configuration, where for each mode in the measurement basis there is one adjacent pump tone.

The Gaussian state of the probe modes is characterized by the correlation matrix. The five-mode correlation matrices for the I and Q quadratures obtained in the dual pump measurement scheme is shown in

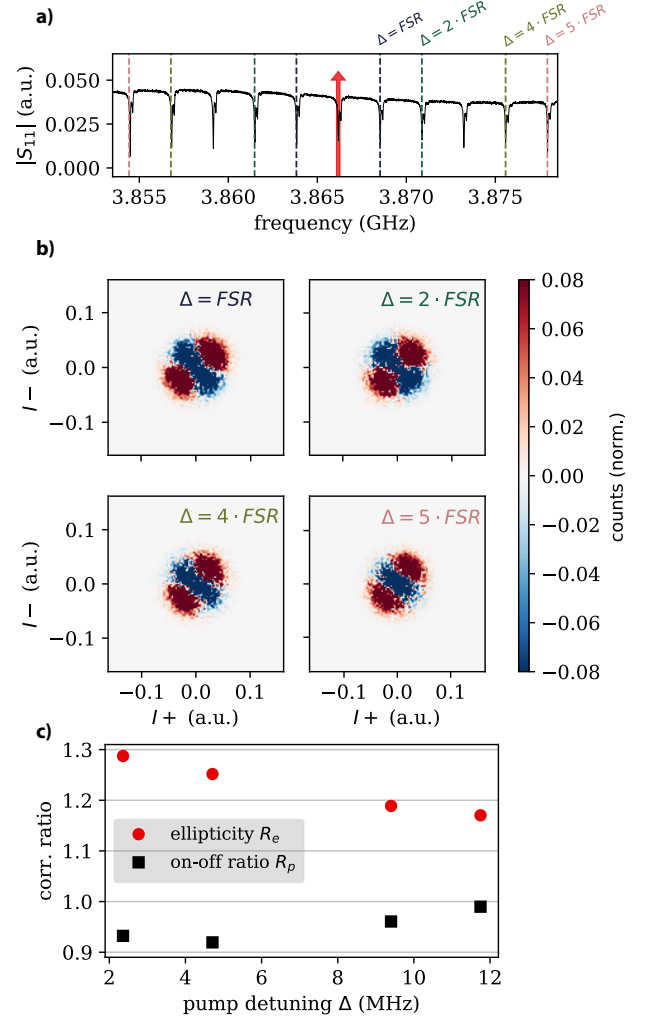


FIG. 3. **Two-mode squeezing.** **a)** Measurement configuration where the red arrow indicates the pump frequency. Dashed lines indicate probe frequencies for collecting quadrature noise data. **b)** Histograms of two-mode correlation data where the measurement with the pump turned off has been subtracted. The label I_+ (I_-) denotes the I quadrature of modes at frequencies above (below) the pump frequency. The label Δ indicates the detuning of the modes from the pump. **c)** Squeezing ellipticity and ratio of standard deviations of the noise in the squeezed quadrature relative to the pump-off case. The quantities are plotted as a function of detuning of the measured mode pair from the pump. All modes show squeezing below the pump off level, and the error bars are smaller than the plot markers.

Fig. 4. Similarly to the single-pump measurement, a mode-selective quadrature rotation is applied that compensates for phase drift in the experiment. In addition, each mode is quadrature-rotated to eliminate correlations of the form $\langle I_j Q_k \rangle$, $j \neq k$, and yield separate correlation matrices for I and Q . The diagonal pump-off level correlations are then subtracted such that the correlation

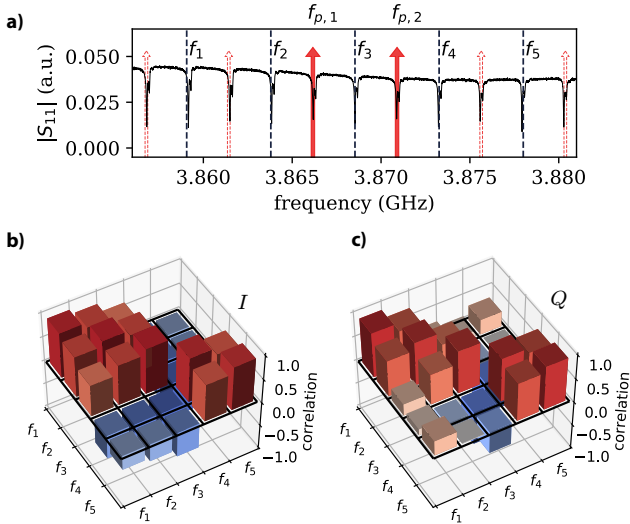


FIG. 4. Two-pump multimode correlation measurement. **a)** Measurement configuration where the solid red arrows indicate the pump frequencies. Dashed lines indicate probe frequencies for collecting quadrature noise data. The nonlinearity of the device gives rise to intermodulation products at frequencies $f_{IMP} = n_1 f_{p,1} + n_2 f_{p,2}$ which also contribute to pumping. These are indicated by the red outline arrows. **b)** Five-mode correlation matrix for the I quadrature generated from quadrature data in the dual pump scheme. The corresponding matrix for the Q quadrature is shown in **c)**.

matrix elements for the I quadrature are

$$C_{jk}^I = \frac{\langle I_j I_k \rangle - \langle I_{j,off} I_{k,off} \rangle}{\sqrt{\langle I_j \rangle^2 \langle I_k \rangle}}. \quad (6)$$

The correlation matrix C_{jk}^Q is analogously defined.

The histograms of the output quadratures for the f_k modes are all measured in parallel. In this case the correlations are not restricted to pairwise two-mode squeezing, but all modes are mutually correlated. Modes closer in frequency show stronger intermode correlations and the weakest correlations appear between modes f_1 and f_5 .

Minimal variance in relation to the pump-off case is now observed in a basis consisting of a linear combination of all the measured quadratures [10]. In contrast to the two-mode squeezing data obtained with a single pump, this minimal variance obtained in the two-pump measurement does not go below the pump off level. A plausible explanation is that this is not caused by excess noise in the dual pump experiment, but the fact that the pump induces correlations also with respect to modes outside the measured five-mode set. A full state reconstruction would require including also these modes in measurement and analysis. Extending the measure-

ment scheme to observe cluster-state entanglement with sizes approaching the number of modes in the SAW resonator is possible using the current setup, as it only requires sampling a larger set of modes and tailoring the pump amplitudes to contain correlations inside the cluster. The digital control of the amplitude and phase of each pump tone should enable precise engineering of the correlation structure.

VI. CONCLUSIONS

We have demonstrated two-mode squeezing of the phononic vacuum in a multi-mode surface acoustic wave resonator. Extending this scheme with a second pump tone, we have observed correlations between additional resonator mode pairs, demonstrating that complex entanglement structures are in principle achievable in this device. Using a digitally synthesized microwave frequency comb as the pump, the generation of phononic cluster states for continuous variable quantum computing can be implemented in this platform. The dense mode structure of the resonator enables multiplexing all modes to one measurement channel without analog frequency conversion. The small on-chip footprint of our device ($< 0.2 \text{ mm}^2$) further contributes to scalability.

A prospect for further development is the integration of superconducting qubits into the resonator, enabling non-Gaussian operations in continuous variable encodings of quantum information such as the addition or subtraction of single phonons. Non-Gaussianity is important to many applications [37] and qubit-controlled operations on the resonator state are more readily implemented in a circuit QED setting than optical experiments where nonlinearities are typically weaker.

Another promising application for this device is in quantum simulation using the resonator modes as lattice sites in a synthetic dimension. Modulating the reflector SQUID at a frequency corresponding to the the free spectral range will induce nearest-neighbour hopping of phonons, giving rise to an effective lattice Hamiltonian in a hardware-efficient way.

VII. ACKNOWLEDGEMENTS

We acknowledge IARPA and Lincoln Labs for providing the TWPA used in this experiment. We are grateful to V. Shumeiko and G. Ferrini for fruitful discussions. This work was supported by the Knut and Alice Wallenberg foundation through the Wallenberg Center for Quantum Technology (WACQT), and the Swedish Research Council, VR.

[1] M. H. Devoret and R. J. Schoelkopf, *Science* **339**, 1169 (2013).

[2] J. M. Gambetta, J. M. Chow, and M. Steffen, *npj Quantum Information* **3**, 2 (2017).

[3] G. Wendin, *Reports on Progress in Physics* **80**, 106001 (2017).

[4] S. Puri, C. K. Andersen, A. L. Grimsom, and A. Blais, *Nature Communications* **8**, 15785 (2017).

[5] M. Kounalakis, C. Dickel, A. Bruno, N. K. Langford, and G. A. Steele, *npj Quantum Information* **4**, 38 (2018).

[6] C. Weedbrook, S. Pirandola, N. J. Cerf, and T. C. Ralph, *Reviews of Modern Physics* **84**, 621 (2012).

[7] O. Pfister, *Journal of Physics B: Atomic, Molecular and Optical Physics* **53**, 012001 (2020).

[8] S. T. Flammia, N. C. Menicucci, and O. Pfister, *Journal of Physics B: Atomic, Molecular and Optical Physics* **42**, 114009 (2009).

[9] M. Chen, N. C. Menicucci, and O. Pfister, *Phys. Rev. Lett.* **112**, 120505 (2014).

[10] R. Medeiros De Araújo, J. Roslund, Y. Cai, G. Ferrini, C. Fabre, and N. Treps, *Physical Review A - Atomic, Molecular, and Optical Physics* **89**, 053828 (2014).

[11] J. Yoshikawa, S. Yokoyama, T. Kaji, C. Sornphiphatphong, Y. Shiozawa, K. Makino, and A. Furusawa, *APL Photonics* **1**, 060801 (2016).

[12] M. V. Larsen, X. Guo, C. R. Breum, J. S. Neergaard-Nielsen, and U. L. Andersen, *Science* **366**, 369 (2019).

[13] W. Asavanant, Y. Shiozawa, S. Yokoyama, B. Charoensombutamon, H. Emura, R. N. Alexander, S. Takeda, J. ichi Yoshikawa, N. C. Menicucci, H. Yonezawa, and A. Furusawa, *Science* **366**, 373 (2019).

[14] B. Vlastakis, G. Kirchmair, Z. Leghtas, S. E. Nigg, L. Frunzio, S. M. Girvin, M. Mirrahimi, M. H. Devoret, and R. J. Schoelkopf, *Science* **342**, 607 (2013).

[15] S. Rosenblum, P. Reinhold, M. Mirrahimi, L. Jiang, L. Frunzio, and R. J. Schoelkopf, *Science* **361**, 266 (2018).

[16] A. Roy and M. Devoret, *Comptes Rendus Physique* **17**, 740 (2016).

[17] V. V. Sivak, S. Shankar, G. Liu, J. Aumentado, and M. H. Devoret, *Phys. Rev. Applied* **13**, 024014 (2020).

[18] P. Lähteenmäki, G. S. Paraoanu, J. Hassel, and P. J. Hakonen, *Nature Communications* **7**, 12548 (2016).

[19] C. W. Sandbo Chang, M. Simoen, J. Aumentado, C. Sabín, P. Forn-Díaz, A. M. Vadhiraj, F. Quijandría, G. Johansson, I. Fuentes, and C. M. Wilson, *Physical Review Applied* **10**, 044019 (2018).

[20] F. Arute, K. Arya, R. Babbush, D. Bacon, J. C. Bardin, R. Barends, R. Biswas, S. Boixo, F. G. Brandao, D. A. Buell, B. Burkett, Y. Chen, Z. Chen, B. Chiaro, R. Collins, W. Courtney, A. Dunsworth, E. Farhi, B. Foxen, A. Fowler, C. Gidney, M. Giustina, R. Graff, K. Guerin, S. Habegger, M. P. Harrigan, M. J. Hartmann, A. Ho, M. Hoffmann, T. Huang, T. S. Humble, S. V. Isakov, E. Jeffrey, Z. Jiang, D. Kafri, K. Kechedzhi, J. Kelly, P. V. Klimov, S. Knysh, A. Korotkov, F. Kostritsa, D. Landhuis, M. Lindmark, E. Lucero, D. Lyakh, S. Mandrà, J. R. McClean, M. McEwen, A. Megrant, X. Mi, K. Michielsen, M. Mohseni, J. Mutus, O. Naaman, M. Neeley, C. Neill, M. Y. Niu, E. Ostby, A. Petukhov, J. C. Platt, C. Quintana, E. G. Rieffel, P. Roushan, N. C. Rubin, D. Sank, K. J. Satzinger, V. Smelyanskiy, K. J. Sung, M. D. Trevithick, A. Vainsencher, B. Villalonga, T. White, Z. J. Yao, P. Yeh, A. Zalcman, H. Neven, and J. M. Martinis, *Nature* **574**, 505 (2019).

[21] A. Mari and J. Eisert, *Physical Review Letters* **109**, 230503 (2012).

[22] B. A. Moores, L. R. Sletten, J. J. Viennot, and K. W. Lehnert, *Physical Review Letters* **120**, 227701 (2018).

[23] L. R. Sletten, B. A. Moores, J. J. Viennot, and K. W. Lehnert, *Physical Review X* **9**, 21056 (2019).

[24] G. Andersson, A. L. O. Bilobran, M. Scigliuzzo, M. M. de Lima, J. H. Cole, and P. Delsing, (2020), arXiv:2002.09389.

[25] Y. Chu, P. Kharel, W. H. Renninger, L. D. Burkhardt, L. Frunzio, P. T. Rakich, and R. J. Schoelkopf, *Science* **358**, 199 (2017).

[26] K. J. Satzinger, Y. P. Zhong, H. S. Chang, G. A. Pairs, A. Bienfait, M. H. Chou, A. Y. Cleland, C. R. Conner, Dumur, J. Grebel, I. Gutierrez, B. H. November, R. G. Povey, S. J. Whiteley, D. D. Awschalom, D. I. Schuster, and A. N. Cleland, *Nature* **563**, 661 (2018).

[27] M. Kervinen, J. E. Ramírez-Muñoz, A. Välimäa, and M. A. Sillanpää, *Phys. Rev. Lett.* **123**, 240401 (2019).

[28] C. T. Hann, C.-l. Zou, Y. Zhang, Y. Chu, R. J. Schoelkopf, S. M. Girvin, and L. Jiang, *Physical Review Letters* **123**, 250501 (2019).

[29] N. R. A. Lee, M. Pechal, E. A. Wollack, P. Arrangoiz-Arriola, Z. Wang, and A. H. Safavi-Naeini, *Phys. Rev. A* **101**, 053807 (2020).

[30] S. Datta, *Surface Acoustic Wave Devices* (Prentice Hall, Englewood Cliffs, N.J., 1986).

[31] T. Genji and J. Kondoh, in *2014 IEEE International Frequency Control Symposium (FCS)* (2014) pp. 1–4.

[32] <https://intermodulation-products.com/products/vivace> (2020).

[33] See supplementary material.

[34] D. C. McKay, S. Philipp, A. Mezzacapo, E. Magesan, J. M. Chow, and J. M. Gambetta, *Physical Review Applied* **6**, 064007 (2016).

[35] F. Yan, P. Krantz, Y. Sung, M. Kjaergaard, D. L. Campbell, T. P. Orlando, S. Gustavsson, and W. D. Oliver, *Physical Review Applied* **10**, 054062 (2018).

[36] C. Macklin, K. O'Brien, D. Hover, M. E. Schwartz, V. Bolkhovsky, X. Zhang, W. D. Oliver, and I. Siddiqi, *Science* **350**, 307 (2015).

[37] Y. S. Ra, A. Dufour, M. Walschaers, C. Jacquard, T. Michel, C. Fabre, and N. Treps, *Nature Physics* **16**, 144 (2019).

**Supplementary Materials:
Squeezing and correlations of multiple modes in a parametric acoustic cavity**

Gustav Andersson,^{1,*} Shan W. Jolin,² Marco Scigliuzzo,¹ Riccardo Borgani,² Mats O. Tholén,^{2,3} David B. Haviland,² and Per Delsing¹

¹*Department of Microtechnology and Nanoscience MC2,*

Chalmers University of Technology, SE-41296 Göteborg, Sweden

²*Nanostructure Physics, KTH Royal Institute of Technology, SE-10691 Stockholm, Sweden*

³*Intermodulation Products AB, SE-82393 Segersta, Sweden*

(Dated: November 18, 2021)

* gustav.andersson@chalmers.se

I. MICROWAVE MULTIFREQUENCY LOCK-IN AMPLIFIER

A schematic illustrating the measurement setup is shown in Fig. S1. A key component is the all-digital microwave measurement platform called Vivace [1]. It has 8 channels of high speed digital-to-analog (DAC) and analog-to-digital converters (ADC) serviced by a large field programmable gate array (FPGA), all synchronized to one stable clock. Vivace can digitally synthesize drive signals and digitize response signals in the band 2-4 GHz, without analog IQ mixers. We set the sampling clock at 4 GSamples/s for the ADCs, and at 5 GSamples/s for the DACs, resulting in a Nyquist frequency of 2 GHz and 2.5 GHz respectively. The SAW cavity modes are designed to fall in the band 3.8 - 3.9 GHz, as this places us within the second Nyquist bands of the converters.

To reach this band we start by synthesizing signals in the band 0-250 MHz. We then perform digital IQ mixing with a numerically controlled oscillator followed by multiplication with the sampling clock inside the converter [2]. Downconversion is performed in an analogous manner. This process embodies all-digital IQ mixing with a virtual local oscillator (VLO), specified by the user. For all our correlation experiments, we set the VLO to 3.8 GHz to access the band 3.8 ± 0.250 GHz. Due to the digital nature of the mixing process, the upper and lower sidebands can be perfectly suppressed and there is no VLO leakage. Any generated spurious aliased tones outside the band are removed with external analog filters.

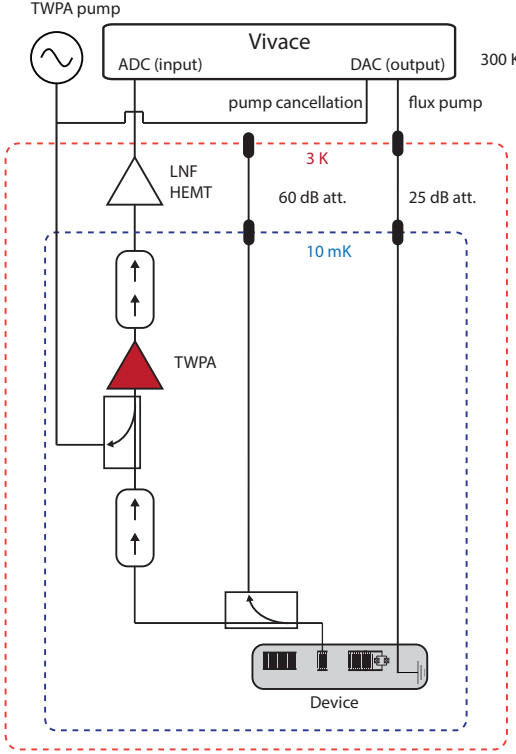


FIG. S1. **Schematic of the measurement setup.** To avoid crosstalk from the flux pump line saturating the TWPA, we use a destructively interfering cancellation tone at the pump frequency. This cancellation tone is output from a separate channel on Vivace and combined with the TWPA pump.

Firmware on the FPGA realizes a synchronous multifrequency lockin amplifier [3] which can drive and measure response at 32 frequencies simultaneously. An essential feature is the phase-coherent nature of the multifrequency measurement.

II. PARAMETRIC COUPLING MODEL

A. Hamiltonian

In this model we consider the coupling induced between linear SAW modes by the common interaction with the *LC* resonance of the mirror under parametric modulation. We will assume that the mirror mode remains in the ground

state and model it as a qubit. The total Hamiltonian is a sum of three terms, $H = H_q + H_{\text{SAW}} + H_{\text{int}}$ given by

$$H_q = \frac{\omega_q \sigma_z}{2}, \quad (\text{S1})$$

$$H_{\text{SAW}} = \sum_i \omega_i b_i^\dagger b_i, \quad (\text{S2})$$

$$H_{\text{int}} = \sum_i g (\sigma_- + \sigma_+) (b_i + b_i^\dagger). \quad (\text{S3})$$

We transform the Hamiltonian to the dispersive regime by applying the unitary transformation $e^S H e^{-S}$ with

$$S = \sum_i \left[\lambda_i (\sigma_+ b_i - \sigma_- b_i^\dagger) + \eta_i (\sigma_- b_i - \sigma_+ b_i^\dagger) \right]. \quad (\text{S4})$$

Note that we are not at this point discarding any counter-rotating terms. Evaluating the commutators for the SAW and mirror modes we obtain

$$[S, H_q] = \left[\lambda_i (\sigma_+ b_i - \sigma_- b_i^\dagger), \frac{\omega_q \sigma_z}{2} \right] + \left[\eta_i (\sigma_- b_i - \sigma_+ b_i^\dagger), \frac{\omega_q \sigma_z}{2} \right] \quad (\text{S5})$$

$$= \sum_i \lambda_i \omega_q (\sigma_+ b_i + \sigma_- b_i^\dagger) + \sum_i \eta_i \omega_q (\sigma_+ b_i^\dagger + \sigma_- b_i), \quad (\text{S6})$$

$$[S, H_{\text{SAW}}] = \left[\lambda_i (\sigma_+ b_i - \sigma_- b_i^\dagger), \sum_i \omega_i b_i^\dagger b_i \right] + \left[\eta_i (\sigma_- b_i - \sigma_+ b_i^\dagger), \sum_i \omega_i b_i^\dagger b_i \right] \quad (\text{S7})$$

$$= - \sum_i \lambda_i \omega_i (\sigma_+ b_i + \sigma_- b_i^\dagger) + \sum_i \eta_i \omega_i (\sigma_+ b_i^\dagger + \sigma_- b_i). \quad (\text{S8})$$

For the interaction term we use the relation $[A, BC] = [A, B]C + B[A, C]$ and get

$$[S, H_{\text{int}}] = \left[\lambda_i (\sigma_+ b_i - \sigma_- b_i^\dagger), \sum_i g (\sigma_- + \sigma_+) (b_i + b_i^\dagger) \right] + \left[\eta_i (\sigma_- b_i - \sigma_+ b_i^\dagger), \sum_i g (\sigma_- + \sigma_+) (b_i + b_i^\dagger) \right] \quad (\text{S9})$$

$$= \sum_{i,j} \lambda_i g \sigma_z (b_i + b_i^\dagger) (b_j + b_j^\dagger) + \sum_i \lambda_i g (\sigma_+ + \sigma_-)^2 + \quad (\text{S10})$$

$$- \sum_{i,j} \eta_i g \sigma_z (b_i + b_i^\dagger) (b_j + b_j^\dagger) + \sum_i \eta_i g (\sigma_+ + \sigma_-)^2 \quad (\text{S11})$$

$$= \sum_{i,j} g \sigma_z (\lambda_i - \eta_i) (b_i + b_i^\dagger) (b_j + b_j^\dagger) + \sum_i g (\lambda_i + \eta_i) (\sigma_+ + \sigma_-)^2. \quad (\text{S12})$$

If we choose $\lambda_i = g / (\omega_q - \omega_i)$ and $\eta_i = g / (\omega_q + \omega_i)$, we obtain

$$[S, H_q + H_{\text{SAW}}] = -H_{\text{int}}. \quad (\text{S13})$$

From the Baker-Hausdorff formula we have

$$e^S H e^{-S} = H + [S, H] + \frac{1}{2!} [S, [S, H]] + \dots \quad (\text{S14})$$

$$= H_q + H_{\text{SAW}} + H_{\text{int}} + [S, H_{\text{int}}] - H_{\text{int}} + \frac{1}{2!} [S, -H_{\text{int}} + [S, H_{\text{int}}]] + \dots \quad (\text{S15})$$

$$= H_q + H_{\text{SAW}} + \frac{1}{2} [S, H_{\text{int}}] + \dots \quad (\text{S16})$$

Assuming the mirror remains in the ground state ($\sigma_z = -1, \sigma_+ \sigma_- = 0$), we end up with the dispersive Hamiltonian

$$H = \sum_i \left[\omega_i b_i^\dagger b_i + \frac{g^2}{2} \left(\frac{1}{\omega_q - \omega_i} + \frac{1}{\omega_q + \omega_i} \right) (\sigma_+^2 + \sigma_-^2) \right] - \frac{g^2}{2} \sum_{i,j} \left(\frac{1}{\omega_q - \omega_i} - \frac{1}{\omega_q + \omega_i} \right) (b_i + b_i^\dagger) (b_j + b_j^\dagger). \quad (\text{S17})$$

Defining $\tilde{g}_i = g^2 (1/(\omega_q - \omega_i) - 1/(\omega_q + \omega_i))$ and $\bar{g}_i = g^2 (1/(\omega_q - \omega_i) + 1/(\omega_q + \omega_i))$ turns the Hamiltonian into

$$H = \sum_i \left[\omega_i b_i^\dagger b_i + \frac{\bar{g}_i}{2} (\sigma_+^2 + \sigma_-^2) \right] - \frac{1}{2} \sum_{i,j} \tilde{g}_i (b_i + b_i^\dagger) (b_j + b_j^\dagger) \quad (\text{S18})$$

which retains single and two-mode squeezing terms.

B. Flux modulation of \tilde{g}_i

The superconducting quantum interference device (SQUID) embedded in one of the Bragg reflectors, forms a lumped element LC circuit with a frequency $\omega_{LC} = 1/\sqrt{L_J C}$ where C is the capacitance dominated by the interdigitated transducers (IDT) of the Bragg reflector and L_J is the Josephson inductance

$$L_J = \frac{\hbar}{2eI_m}, \quad (\text{S19})$$

e is the elementary charge and I_m is the maximum supercurrent through the SQUID. The mirror frequency can therefore be expressed as

$$\omega_{LC} = \sqrt{\frac{2eI_m}{\hbar C}}. \quad (\text{S20})$$

The mirror frequency ω_{LC} is tunable since I_m depends on the external magnetic flux Φ_p . In the case where the SQUID consists of two identical junctions, each characterized by a critical current I_c , the maximum supercurrent can be expressed as [4]

$$I_m = 2I_c |\cos(\pi\Phi_p/\Phi_0)|. \quad (\text{S21})$$

In our case, Φ_p is supplied by our pump

$$\Phi_p(t) = \Phi_{AC} \cos(\omega_p t + \phi_p), \quad (\text{S22})$$

and, as a consequence, the mirror frequency ω_{LC} also acquires a time dependence. Inserting Eq. (S21) into Eq. (S20) provides the expression for the mirror frequency as a function of external flux

$$\omega_{LC}(\Phi_p) = \omega_{LC}(0) \sqrt{|\cos(\pi\Phi_p/\Phi_0)|}, \quad (\text{S23})$$

$$\omega_{LC}(0) = \sqrt{\frac{4eI_c}{\hbar C}} \quad (\text{S24})$$

and we assume henceforth that $-\pi/2 < \pi\Phi_p(t)/\Phi_0 < \pi/2$.

The presence of a time-varying flux will also affect \tilde{g}_i , which couples the SAW modes. Inserting our expression for $\omega_{LC}(\Phi_p)$ from Eq. (S23) into Eq. (2) in the main text, results in

$$\tilde{g}_i = g^2 \left(\frac{1}{\Omega_{LC} \sqrt{\cos x} - \omega_i} - \frac{1}{\Omega_{LC} \sqrt{\cos x} + \omega_i} \right). \quad (\text{S25})$$

Here we introduce the shorthand notation $x = \pi\Phi_p(t)/\Phi_0$ and $\Omega_{LC} = \omega_{LC}(0)$ to indicate the mirror frequency in the absence of external flux.

For $\Phi_{AC} \ll \Phi_0$, we Taylor expand around $x \approx 0$ up to second order to obtain

$$\tilde{g}_i = \frac{g^2 \omega_i}{\Omega_{LC}^2 - \omega_i^2} \left(2 + \frac{\Omega_{LC}^2}{2(\Omega_{LC}^2 - \omega_i^2)} x^2 \right)$$

By reintroducing $x = \pi\Phi_p(t)/\Phi_0 = \pi\Phi_{AC} \cos(\omega_p t + \phi_p)/\Phi_0$, we finally arrive at the coupling \tilde{g}_i in the regime of small Φ_{AC}

$$\tilde{g}_i = \frac{g^2 \omega_i}{\Omega_{LC}^2 - \omega_i^2} \left(2 + \frac{\Omega_{LC}^2}{2(\Omega_{LC}^2 - \omega_i^2)} \frac{\pi^2 \Phi_{AC}^2}{2\Phi_0^2} (\cos(2\omega_p t + 2\theta_p) + 1) \right). \quad (\text{S26})$$

The expression can be split into time-dependent and time-independent parts $\tilde{g}_i = \tilde{g}_{i,0} + \tilde{g}_{i,1} \cos(2\omega_p t + 2\theta_p)$ where

$$\begin{aligned}\tilde{g}_{i,0} &= \frac{2g^2\omega_i}{\Omega_{LC}^2 - \omega_i^2} + \frac{g^2\omega_i\Omega_{LC}^2}{4(\Omega_{LC}^2 - \omega_i^2)^2} \frac{\pi^2\Phi_{AC}^2}{\Phi_0^2}, \\ \tilde{g}_{i,1} &= \frac{g^2\omega_i\Omega_{LC}^2}{4(\Omega_{LC}^2 - \omega_i^2)^2} \frac{\pi^2\Phi_{AC}^2}{\Phi_0^2}.\end{aligned}$$

For convenience however, we will instead express the coupling term as

$$\tilde{g}_i = \alpha_i + \beta_i \left(\frac{e^{2j(\omega_p t + \theta_p)} + e^{-2j(\omega_p t + \theta_p)}}{2} + 1 \right), \quad (\text{S27})$$

where

$$\begin{aligned}\alpha_i &= \tilde{g}_{i,0} - \tilde{g}_{i,1}, \\ \beta_i &= \tilde{g}_{i,1}.\end{aligned}$$

In the rotating wave approximation (RWA), α_i will provide a constant shift to the SAW resonances while β_i , which depends on the coupling, detuning and pump amplitude, will determine the interaction strength and therefore also the amount of squeezing.

III. CALCULATING THE COVARIANCE MATRIX

The covariance matrix of the outgoing radiation leaking out from the SAW modes through the IDT can be calculated from the Hamiltonian (S18). We will consider the case of three SAW modes: a pump mode b_p with resonance frequency ω_p , flanked by two other modes b_- and b_+ with resonance frequencies ω_- and ω_+ respectively. The resonances satisfy approximately $2\omega_p \sim \omega_- + \omega_+$. In the case of a strong pump applied at frequency $\nu_p \sim \omega_p$ and if the following hierarchy of scales $\omega_p \gg FSR \gg \alpha_i, \beta_i$ are true, a rotating wave approximation (RWA) of Eq. (S18) results in

$$H_{\text{RWA}} = \sum_i (\Omega_i - \beta_i) b_i^\dagger b_i - \frac{1}{4} \sum_{i \neq j} \sum_{j \neq i} \beta_i \left(e^{-2j\nu_p t - 2j\theta_p} b_i^\dagger b_j^\dagger + e^{2j\nu_p t + 2j\theta_p} b_i b_j \right), \quad (\text{S28})$$

where

$$\Omega_i = \omega_i - \frac{1}{2} \alpha_i$$

are the dressed SAW resonances. The subindices i and j above refer to the three modes $\{-, p, +\}$. Using the methods of Gardiner and Collett [5], the equation of motion for the b_- mode can be written:

$$\dot{b}_- = -j \left(\Omega_- - \beta_- - j \frac{\kappa_{c,-} + \kappa_{i,-}}{2} \right) b_- + j \frac{\beta_- + \beta_+}{4} e^{-2j\theta_p} b_+^\dagger + \sqrt{\kappa_{c,-}} b_-^{\text{in}} + \sqrt{\kappa_{i,-}} b_-^{\text{loss}}. \quad (\text{S29})$$

Each SAW cavity is coupled to their environment through a linear dissipation port with rate $\kappa_{i,-}$ and an accessible test port (coupled through the IDT) with rate $\kappa_{c,-}$, with their corresponding quality factors given by $Q_{i,-} = \Omega_- / \kappa_{i,-}$ and $Q_{c,-} = \Omega_- / \kappa_{c,-}$. The terms b_-^{loss} and b_-^{in} indicate the incoming noise from the dissipation and test port respectively. For the b_+ mode, we interchange indices $+\leftrightarrow-$ in the above expression.

We use the following definition of the Fourier transform

$$g[\nu] = \frac{1}{\sqrt{2\pi}} \int_{-\infty}^{\infty} g(t) e^{j\nu t} \quad (\text{S30})$$

$$g(t) = \frac{1}{\sqrt{2\pi}} \int_{-\infty}^{\infty} g[\nu] e^{-j\nu t} \quad (\text{S31})$$

to transform the equation of motion for the b_- and b_+ modes into the frequency domain. The resulting system of equations can be conveniently cast into the form

$$\vec{S}k = E_{\text{in}} \vec{a}_{\text{in}} + E_{\text{loss}} \vec{a}_{\text{loss}} \quad (\text{S32})$$

where

$$S = \begin{pmatrix} j \left(\Omega_- - \beta_- - \nu_- - j \frac{\kappa_{c,-} + \kappa_{i,-}}{2} \right) & j \frac{\beta_- + \beta_+}{4} e^{-2j\theta_p} \\ -j \frac{\beta_- + \beta_+}{4} e^{2j\theta_p} & -j \left(\Omega_+ - \beta_+ - \nu_+ + j \frac{\kappa_{c,+} + \kappa_{i,+}}{2} \right) \end{pmatrix},$$

$$E_{\text{in}} = \text{diag}(\sqrt{\kappa_{c,-}}, \sqrt{\kappa_{c,+}}),$$

$$E_{\text{loss}} = \text{diag}(\sqrt{\kappa_{i,-}}, \sqrt{\kappa_{i,+}}),$$

$$\vec{k} = (b_-[\nu_-], b_+^\dagger[\nu_+])^T,$$

$$\vec{a}_{\text{in}} = (b_-^{\text{in}}[\nu_-], b_+^{\text{in}\dagger}[\nu_+])^T,$$

$$\vec{a}_{\text{loss}} = (b_-^{\text{loss}}[\nu_-], b_+^{\text{loss}\dagger}[\nu_+])^T.$$

The probe frequencies ν_- and ν_+ strictly satisfy the 4-wave mixing criterion $2\nu_p = \nu_- + \nu_+$.

Through the input-output relations, the outgoing radiation is

$$b_-^{\text{out}} = \sqrt{\kappa_{c,-}} b_- - b_-^{\text{in}}, \quad (\text{S33})$$

which can also be cast in the form

$$\vec{a}_{\text{out}} = E_{\text{in}} \vec{k} - \vec{a}_{\text{in}} \quad (\text{S34})$$

where we analogously define

$$\vec{a}_{\text{out}} = (b_-^{\text{out}}[\nu_-], b_+^{\text{out}\dagger}[\nu_+])^T.$$

The b_-^{out} and b_+^{out} are the outgoing noise terms leaving through the IDT. Combining Eq. (S32) and (S34) results in:

$$\vec{a}_{\text{out}} = (E_{\text{in}} S^{-1} E_{\text{in}} - I) \vec{a}_{\text{in}} + E_{\text{in}} S^{-1} E_{\text{loss}} \vec{a}_{\text{loss}}. \quad (\text{S35})$$

As a final step before calculating the covariance matrix, we compute the quantity $A_{\text{out}} = \langle \vec{a}_{\text{out}} \vec{a}_{\text{out}}^T \rangle$ by using Eq. (S35)

$$A_{\text{out}} = ((E_{\text{in}} \oplus E_{\text{in}}) M^{-1} (E_{\text{in}} \oplus E_{\text{in}}) - I) A_{\text{in}} ((E_{\text{in}} \oplus E_{\text{in}}) (M^{-1})^T (E_{\text{in}} \oplus E_{\text{in}}) - I) \\ + (E_{\text{in}} \oplus E_{\text{in}}) M^{-1} (E_{\text{loss}} \oplus E_{\text{loss}}) A_{\text{loss}} (E_{\text{loss}} \oplus E_{\text{loss}}) (M^{-1})^T (E_{\text{in}} \oplus E_{\text{in}}), \quad (\text{S36})$$

where M is a block diagonal matrix

$$M = S \oplus S^* = \begin{pmatrix} S & 0 \\ 0 & S^* \end{pmatrix}.$$

The matrices A_{in} and A_{loss} are defined as

$$A_{\text{in}} = A_{\text{loss}} = \begin{pmatrix} 0 & 0 & \bar{n} + 1 & 0 \\ 0 & 0 & 0 & \bar{n} \\ \bar{n} & 0 & 0 & 0 \\ 0 & \bar{n} + 1 & 0 & 0 \end{pmatrix}$$

where \bar{n} as the mean number of photons per unit bandwidth, set by the temperature of the phonon environment.

Finally, the covariance matrix V is calculated as

$$V = \frac{(P A_{\text{out}} P^T)^T + P A_{\text{out}} P^T}{2} \quad (\text{S37})$$

defined such that $(V)_{ij} = \frac{1}{2} \langle \{A_i, A_j\} \rangle$, where $A = (I_-, Q_-, I_+, Q_+)^T$. Notice that we use the IQ -notation instead of the common qp - or xp -notation. The matrix P , defined as

$$P = \begin{pmatrix} 1 & 0 & 1 & 0 \\ -j & 0 & j & 0 \\ 0 & 1 & 0 & 1 \\ 0 & j & 0 & -j \end{pmatrix},$$

is necessary to cast V into a form that satisfies the definition.

The covariance matrix V is currently dimensionless and defined for the vacuum state to be the identity matrix at a unit bandwidth. To obtain the covariance matrix in terms of noise power, multiply I and Q (in the definition of V) by $\sqrt{\frac{1}{2}Z_c h f \Delta f}$ where Δf is the measurement bandwidth, f is the center frequency and Z_c is the characteristic impedance of the transmission line.

IV. GAIN AND NOISE ESTIMATE

We model the effect of amplification on the covariance matrix according to [6]

$$V_m = T V T + N \quad (\text{S38})$$

where $T = \sqrt{G} I$ and $N = (G - 1)(2\bar{n}_{\text{add}} + 1) I$. Our amplifier chain is characterized by an effective amplitude gain \sqrt{G} and effective added mean photon number \bar{n}_{add} . The covariance matrix accessible to measurement is given by V_m , while V represents the quantum state. Thus a good estimate of \sqrt{G} and \bar{n}_{add} would allow us to reconstruct the quantum statistics.

There are different methods to calibrate gain and added noise, which typically require a form of calibrated noise source [7] or a temperature sweep [8, 9]. A method to roughly estimate the gain of the amplification chain using only our device is by measuring cross-correlations in a two-mode squeezed state. Assuming the added noise is thermal, the cross-correlations corresponding to squeezing are independent of the added noise but not the amplifier gain. We quantify these correlations by adding the relevant elements of the covariance matrix as

$$C = \sqrt{(V_m)_{13}^2 + (V_m)_{14}^2 + (V_m)_{23}^2 + (V_m)_{24}^2}. \quad (\text{S39})$$

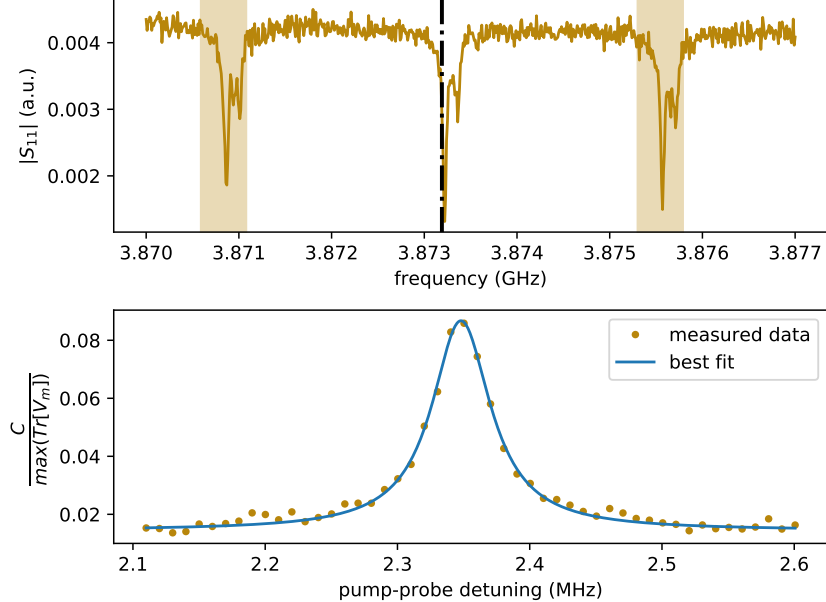


FIG. S2. **Gain estimation.** Top: Frequency sweep depicting the three SAW modes of interest. A pump is positioned at the vertical black dashed line, while noise is measured at frequencies symmetric around the pump, as indicated by the shaded region. Bottom: The correlation quantity C is plotted as a function of pump-probe detuning. A fit to C is made to extract the gain of our amplification chain, assuming an effective phonon temperature of 30 mK. From the fit, we obtain $G \approx 78$ dB, $\beta_- \approx 20$ kHz and $\beta_+ \approx 16$ kHz. For comparison, C is scaled by the maximum measured trace: $\max(\text{Tr}[V_m])$.

We measure C by applying a flux pump at 3.8732 GHz, while measuring the noise in a pair of neighbouring modes. As illustrated in Fig. S2, the pump frequency is placed directly on a SAW mode and probe frequencies are swept across neighbouring SAW modes, always keeping them strictly symmetric with respect to the pump, to satisfy the 4-wave mixing criterion. In Fig. S2, C is plotted as a function of the detuning between the pump and the probe

frequencies. The probe frequency sweep results in a Lorentzian-like shape of C as a function of detuning, where the peak occurs when both probes are located well inside their respective SAW modes.

The C lineshape can be calculated from the expression for the covariance matrix V in Eq. (S37) and applying the transformation (S38) to take amplifiers into account. In order to extract the gain G from a fit to C , it is necessary to specify the SAW mode coupling rates as well as their effective phonon temperature. As the phonon temperature is still required to get an accurate estimate, this method does not do away with standard gain and noise calibration processes. We can, however, use this analysis to obtain an upper bound on the phonon temperature necessary for our measurement to show entanglement.

The fit shown as a solid line in Fig. S2 is extracted assuming a phonon temperature of 30 mK. This yields an estimate of the gain of $G \approx 78$ dB, as well as the squeezing parameters $\beta_- \approx 20$ kHz and $\beta_+ \approx 16$ kHz. This estimated gain lies within range of our expectations. A higher assumed phonon temperature will result in lower estimates of the gain.

The amplifier noise is estimated by solving for \bar{n}_{add} in Eq. (S38), with the gain G obtained from the fit and V_m taken from pump off data, which corresponds to an amplified thermal state with added noise. Here V is given directly by the same assumed temperature as for the gain estimate. Finally, solving for \bar{n}_{add} with these assumptions yields $\bar{n}_{\text{add}} \approx 0.73$. This added noise value is a lower conservative estimate. Using a higher added noise value during reconstruction of V will result in more squeezing.

V. TESTING FOR ENTANGLEMENT

The extracted gain G and noise \bar{n}_{add} allow for reconstruction of the pre-amplified covariance matrix, which is necessary to demonstrate entanglement. Here we apply the partial positive transpose (PPT) criterion [6, 10]. From the two-mode squeezing data (see Fig. S4 or Fig. 3 in the main text), the pre-amplified quantum statistics is obtained by solving for V in Eq. (S38). The reconstructed V is then partially transposed according to

$$\Lambda = \text{diag}(1, 1, 1, -1), \quad (\text{S40})$$

$$\tilde{V} = \Lambda V \Lambda. \quad (\text{S41})$$

We also introduce the symplectic matrix, defined as

$$\Omega = \begin{pmatrix} 0 & 1 & 0 & 0 \\ -1 & 0 & 0 & 0 \\ 0 & 0 & 0 & 1 \\ 0 & 0 & -1 & 0 \end{pmatrix}. \quad (\text{S42})$$

The PPT criterion states that a necessary and sufficient condition for separability for bipartite Gaussian states is that the matrix $H = \tilde{V} + j\Omega$ is positive semidefinite. Thus we test for entanglement by calculating the eigenvalues λ of H and checking whether the smallest eigenvalue λ_{\min} is negative.

The eigenvalues however depend on the phonon temperature, since it affects our estimate of G and \bar{n}_{add} . We take this into account by calculating the value of λ_{\min} at various phonon temperatures, presented in Fig. S3. Accordingly, we observe that entanglement persists for phonon temperatures up to 80 mK. This should be compared to the mixing chamber temperature of 10 mK and previous experiments estimating the effective SAW phonon temperature to 37 mK [11]. Together, these observations suggest that the measured two-mode squeezing is a signature of entangled SAW modes.

VI. TWO-MODE SQUEEZED CORRELATION MATRIX

The two-mode squeezing data obtained with a single pump tone show correlations only between mode pairs symmetric in frequency around the pump. The correlation matrix for the I and Q quadratures of the eight modes sampled in this measurement is shown in Fig. S4. For comparison, we show the covariance matrix for the five modes in the two-pump measurement in Fig. S5.

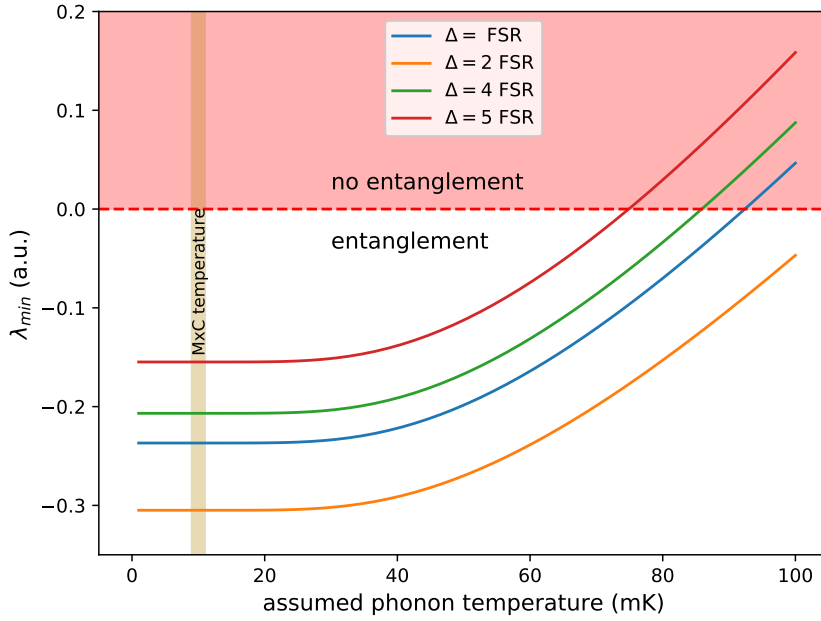


FIG. S3. **PPT criterion results.** We apply the PPT criterion to data presented in Fig. 3 in the main text. We vary the assumed phonon temperature, estimate G and \bar{n}_{add} , and evaluate the PPT criteria at each step. The results suggest entanglement is present up to a phonon temperature of roughly 80 mK.

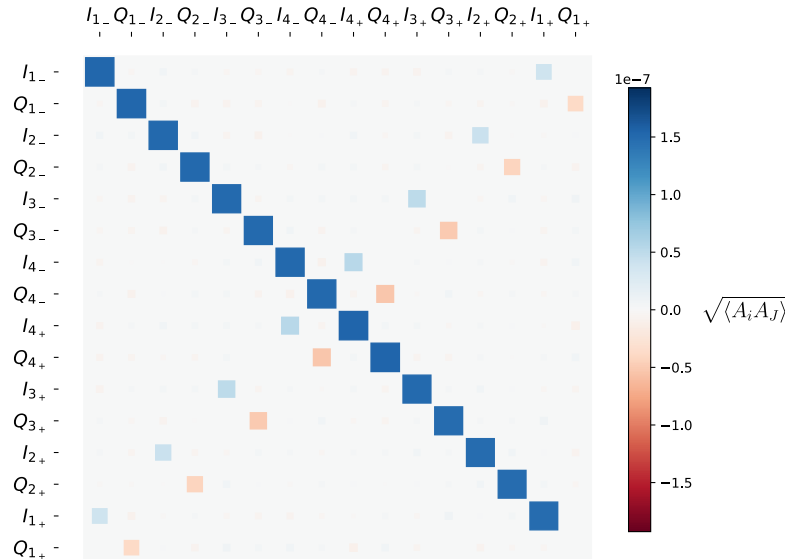


FIG. S4. Covariance matrix (unnormalized) for the single-pump, two-mode squeezing measurement.

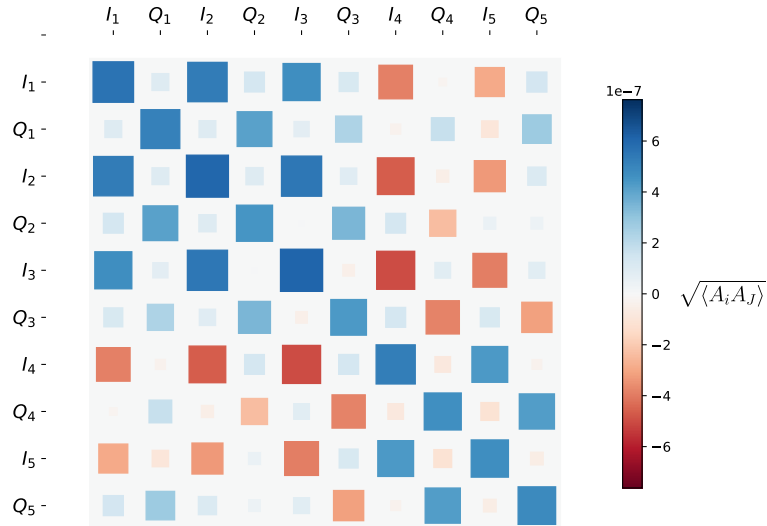


FIG. S5. Covariance matrix (unnormalized) for the two-pump measurement.

- [1] “Intermodulation products AB,” <https://intermodulation-products.com/> (2020).
- [2] “Zynq ultrascale+ rfsoc rfdata converter v2.2,” https://www.xilinx.com/support/documentation/ip_documentation/usp_rf_data_converter/v2_2/pg269-rf-data-converter.pdf (2019).
- [3] E. A. Tholén, D. Platz, D. Forchheimer, V. Schuler, M. O. Tholn, C. Hutter, and D. B. Haviland, *Review of Scientific Instruments* **82**, 026109 (2011).
- [4] M. Tinkham, *Introduction to Superconductivity*, 2nd ed. (Dover Publications, Inc., Mineola, New York, 2004).
- [5] C. W. Gardiner and M. J. Collett, *Physical Review A* **31**, 3761 (1985).
- [6] C. Weedbrook, S. Pirandola, R. Garca-Patr, T. C. Ralph, J. H. Shapiro, and S. Lloyd, *Reviews of Modern Physics* **84**, 621 (2012).
- [7] C. W. Sandbo Chang, M. Simoen, J. Aumentado, C. Sabín, P. Forn-Díaz, A. M. Vadhiraj, F. Quijandría, G. Johansson, I. Fuentes, and C. M. Wilson, *Physical Review Applied* **10**, 044019 (2018).
- [8] E. A. Tholén, *Intermodulation in Microresonators for Microwave Amplification and Nanoscale Surface Analysis*, Ph.D. thesis, KTH Royal Institute of Technology, Stockholm, Sweden (2009), <https://kth.diva-portal.org/smash/record.jsf?pid=diva2%3A277877&dswid=8566>.
- [9] M. Mariantoni, E. P. Menzel, F. Deppe, M. A. Araque Caballero, A. Baust, T. Niemczyk, E. Hoffmann, E. Solano, A. Marx, and R. Gross, *Physical Review Letters* **105**, 133601 (2010).
- [10] R. Simon, *Physical Review Letters* **84**, 2726 (2000).
- [11] A. Noguchi, R. Yamazaki, Y. Tabuchi, and Y. Nakamura, *Physical Review Letters* **119**, 180505 (2017).